Mateo-Mateo, D.; Albero-Sancho, J.; García Gómez, H. (2018). Graphene supported NiO/Ni nanoparticles as efficient photocatalyst for gas phase CO2 reduction with hydrogen. Applied Catalysis B Environmental. 224:563-571. https://doi.org/10.1016/j.apcatb.2017.10.071

Graphene supported NiO/Ni nanoparticles as efficient photocatalyst for gas phase CO_2 reduction with hydrogen

Diego Mateo[a], Josep Albero[a] and Hermenegildo García[a,*]

[a] *Instituto de Tecnología Química, Universitat Politècnica de València-consejo Superior de Investigaciones Científicas, Avenida de los Naranjos s/n, 46022 Valencia, Spain*

Abstract

The photocatalytic activity of NiO/Ni nanoparticles (NPs) supported on defective graphene (NiO/Ni-G) has been tested for the photoassisted CO_2 reduction with H_2. NiO/Ni-G was prepared by H_2 reduction of $NiCl_2$ adsorbed on few-layers defective G and storage under air. An optimal Ni loading of 23 wt% was found, reaching the maximum specific CH_4 formation rate (642 μmol $CH_4 \cdot g_{Ni}^{-1} \cdot h^{-1}$ at 200 ^oC) and quantum yield of 1.98 %. Under the same conditions Ni NPs supported on silica-alumina or NiO NPs exhibit notably lower specific CH_4 production rates than NiO/Ni-G. It was found that H_2O formed in the reaction has a detrimental influence on the photocatalytic activity and evidence supports that H_2O desorption is one of the reasons why the system requires heating. Under continuous flow operation, undesirable water molecules were easier desorbed from the NiO/Ni-G photocatalyst than in the batch mode, reaching a steady specific CH_4 production rate of 244.8 μL $\cdot h^{-1}$ for 50 mg of NiO/Ni-G catalyst with a residence time of 3.1 s. Quenching experiments with electron donor of different oxidation potential (dimethylaniline, anisole and p-xylene) are compatible with a mechanism involving photoinduced charge separation.

Key words: solar fuels, photocatalysis, CO_2 methanation, graphene, Ni nanoparticles

*** Corresponding author.** Tel: +34 96 387 7807; Fax: +34 96 387 7809; E-mail: hgarcia@qim.upv.es

1. Introduction

Much effort is being devoted to develop photocatalysis for the production of solar fuels and particularly to perform CO_2 reduction with a sufficiently high efficiency to compete favorably with conventional catalytic reactions.[1-4] However, in spite of the intense research in the last years in the field, quantum efficiencies and reaction rates for the so-called *artificial photosynthesis* in which CO_2 is reduced by H_2O are much below 1 %, typically in the range of $\mu mol \cdot g_{Cat.}^{-1} \cdot h^{-1}$, still very far from any application.[5-14] Considering the urgency of finding viable solutions for the abatement of CO_2 emissions and implementation of the circular economy for this compound, solar light photocatalysis is moving towards the photoassisted reduction of CO_2 by H_2, since this process can reach specific reaction rates per g of photocatalyst of hundreds of $\mu mols \cdot g^{-1} \cdot h^{-1}$ and apparent quantum yields in the order approaching 1%.[15-20] It is being considered that H_2 can be obtained from renewable electricity by electrolysis and it can become available as reducing chemical for CO_2.[1, 2, 21]

Photoassisted CO_2 reduction by H_2 has been frequently reported using materials containing noble or critical metals, such as Pd, Ru and In in its composition.[15, 17, 18, 20] For the sake of sustainability, it

would be more convenient the use of abundant, non-critical first-raw transition metals in the process, Ni being an obvious candidate considering its availability and the fact that Ni supported on mixed silica alumina (Ni/SiO_2-Al_2O_3) is a commercial catalyst for the thermal CO_2 methanation. CO_2 methanation is one of the few exothermic reactions involving CO_2 as substrate and it can be conveniently carried out in a thermal process using Ni/SiO_2-Al_2O_3 as catalysts at temperatures above 400 ^oC to reach high conversions and rates.[22-26] The advantage of the photoassisted reaction is that it can be performed in the range of temperatures in which the thermal process does not occur or gives only low CO_2 conversions due to the low reaction rates. To shift equilibrium towards the products in an exothermic reaction, low reaction temperatures, but with adequate rates, are more favorable and this could be reached in the photoassisted process.

Continuing with this line of research, it is of much current interest to find other Ni containing materials that can exhibit even higher activity than Ni/SiO_2-Al_2O_3 for the photoassisted CO_2 reduction by H_2 to CH_4 and to gain information about the mechanism of the photo-assisted process. In the present manuscript, it will be reported that NiO/Ni NPs supported on few layers defective graphene (*fl*-G) is a suitable photocatalyst to promote the photoassisted CO_2 reduction by H_2 with specific rates and quantum yields of about 642 $\mu mol \cdot g_{Ni}^{-1} \cdot h^{-1}$ and 1.98 %, respectively. Graphene (G) is a one-atom thick sheet constituted by sp^2 carbons in hexagonal arrangement. Among the unique properties of G besides their high electric and thermal conductivity, others that important from the catalytic point of view are its high specific surface area (about 2500 $m^2 \cdot g^{-1}$)[27] and its strong interaction with supported metal nanoparticles as consequence of the favorable overlap of the extended π orbital of G with the d orbitals of the metal atoms[28]. In addition, G and other 2D related materials have been successfully employed not only as support, but also as additive in catalysts for photocatalytic CO_2 reduction.[29-33] It is, therefore, of interest to demonstrate the general ability of graphenes to increase the photocatalytic activity of active components also for other photoassisted CO_2 reductions. In the present manuscript a defective G material obtained by pyrolysis from a natural polysaccharide that contains carbon vacancies, holes and residual oxygenated functional groups was used. Preparation of this type of defective G from alginate has been already reported in the literature and fully characterization is available [34]. It appears that, as it has been well established in semiconducting photocatalysts,[35-37] the presence of graphene results in a remarkable enhancement of the efficiency of Ni to promote the photoassisted process.

2. Experimental

2.1. Materials and Procedures:

Alginic acid sodium salt from brown algae (Sigma) was pyrolized under argon atmosphere at 900ºC with a heating rate of 10ºC min^{-1} for 2 h to obtain few-layers graphene (fl-G).

Ni NPs were deposited by incipient wetness impregnation, adding dropwise a 10 mL nickel (II) chloride hexahydrate solution over preformed fl-G powders under constant stirring. After this time, the Ni(x)-G (x: wt.% Ni) photocatalyst was filtered and washed with mili Q water and acetone until the complete removal of chloride. The solid catalysts were, then, dried overnight in an oven at 80 °C. The fl-G powders were reduced under H_2 flow (100 $mL \cdot min^{-1}$) at 500 ºC for 2 h with a heating rate of 10 $^oC \cdot min^{-1}$. The resulting material was dried in a vacuum desiccator at 110 ºC to remove the remaining water and stored under ambient atmosphere before its use as photocatalyst.

The amount of nickel present in the samples was determined by inductively coupled plasma-optical

emission spectrometry by immersing the catalysts into aqua regia at room temperature for 12 h and analyzing the Ni content of the resulting solution.

2.2. Characterization:

Powder XRD patterns were recorded on a Shimadzu XRD-7000 diffractometer using Cu Kα radiation (λ = 1.5418 Å, 40 kV, 40 mA) at a scanning speed of 1^0 per min in the 10-80^0 2θ range. Raman spectrum was collected with a Horiba Jobin Yvon-Labram HR UV-Visible NIR (200-1600 nm) Raman microscope spectrometer, using a laser with the wavelength of 512 nm. The spectrum was collected from 10 scans at a resolution of 2 cm^{-1}.
XP spectra were measured on a SPECS spectrometer equipped with a Phoibos 150 9MCD detector using a non-monochromatic X-ray source (Al and Mg) operating at 200 W. The samples were evacuated in the prechamber of the spectrometer at $1 \cdot 10^{-9}$ mbar. The measured intensity ratios of the components were obtained from the area of the corresponding peaks after nonlinear Shirley-type background subtraction and corrected by the transition function of the spectrometer.
TEM images were recorded in a JEOL JEM 2100F under accelerating voltage of 200 kV. Samples were prepared by applying one drop of the suspended material in ethanol onto a carbon-coated copper TEM grid, and allowing them to dry at room temperature.
Diffuse reflectance UV-Vis spectra (DRS) in the range of 200–800 nm were recorded on a Cary 5000 spectrophotometer from Varian.

2.3. Photocatalytic tests:

A photoreactor (51 mL) with a quartz window and a nickel alloy thermocouple was load with Ni(x)-G photocatalyst. H_2 and CO_2 were introduced in stoichiometric amounts up to achieve a final pressure of 1.3 bar. The photoreactor was heated at different temperatures prior irradiation by means of a heating mantle equipped with thermocouple and controller, and when the desired temperature was stabilized the photocatalyst was irradiated with a UV-Vis light from a 300 W Xe lamp. Note that the time required before temperature equilibration can be about 30 min. At that moment the lamp is switched on and this is the initial time of the experiments. No change in the gas phase composition was observed at initial reaction time. The CH_4 formation was followed by direct measurement of the reactor gases with an Agilent 490 MicroGC having two channels both with TC detectors and Ar as carrier gas. One channel has MolSieve 5A column and analyses H_2, O_2, N_2 and CO. The capability of our Micro GC apparatus to detect CO using Ar as carrier gas has been tested using Abell Linder® steel cylinders containing certified N_2:CO mixtures at different concentrations (20, 10 and 5 vol.%) (see **Fig. S1** in supplementary information). The second channel has a Pore Plot Q column and analyses CO_2, CH_4 and up to C_4 hydrocarbons. Quantification of the percentage of each gas was based on prior calibration of the system injecting mixtures with known percentage of gases.

3. Results and discussion

3.1. Photocatalyst preparation and characterization

NiO-Ni NPs supported on *fl*-G with different Ni content were prepared adding different amounts of

hydrated $NiCl_2$ to *fl*-G dispersions, followed by subsequent thermal reduction of Ni^{II} by H_2 atmosphere at 500 ^oC for 2 h. After chemical reductions, the resulting samples were stored under ambient for at least one day before being uses as photocatalyst. This exposure to the ambient can cause some oxidation of the Ni, as it will be discussed below. The Ni content of each sample has been confirmed by ICP-OES elemental analysis. The different samples under study and their respective Ni contents (wt.%) are summarized in **Table 1**.

Table 1. Ni content in the NiO/Ni-G samples, Ni average particle size, total catalyst amount employed and CH_4 production rates obtained at 200 ^oC upon 2236 $W \cdot m^{-2}$ irradiation using a 300 W Xe lamp. P_{H2} = 1.05 bar, P_{CO2} = 0.25 bar.

Sample	Ni [wt %][b]	Size [nm]	Cat. [mg]	CH_4 [$\mu mol \cdot g_{Ni}^{-1} \cdot h^{-1}$]
fl-G	-	-	26.1	0
Ni(6)-G	6.63	-	20	0
Ni(14)-G	14.42	8.0±2.0	25.4	329.05
Ni(23)-G	23.02	8.5±3.5	40	642.66
Ni(23)-G[c]	23.02	8.5±3.5	39.6	0
Ni(23)-G[d]	23.02	8.5±3.5	25.2	0
Ni(26)-G	26.1	13.7±6.0	37	303.09
Ni-Al_2O_3/SiO_2	65	6.2±1.1[e]	14	358.5
NiO	-	< 50	12.7	31.1
NiO-fl-G	23		25.4	69.86
Ni(23)-G[f]	23.02	8.5±3.5	25.5	0

[a] Referred in this case to amount of G; [b] The difference in weight corresponds to the percentage of graphene; [c] Room temperature; [d] Dark conditions; [e] From ref. [38]; [f] Photocatalysts pre-activated under H_2 atmosphere at 200 ^oC for 4 h and subsequent reaction at room temperature under light illumination.

Raman spectroscopy was employed to characterize the defective *fl*-G used as support. The Raman spectrum revealed the typical 2D (2700 cm^{-1}), G (1580 cm^{-1}) and D (1350 cm^{-1}) bands characteristic to the defective G obtained from the pyrolysis of alginate (see **Fig. 1 a**). The defects correspond to carbon vacancies and holes generated by evolution of CO_2 and CO during the pyrolysis and to the presence of residual oxygen (about 7 wt.%) remaining from the composition of the polysaccharide precursor after pyrolysis.

XRD pattern of the Ni(23)-G photocatalyst revealed that the NiO/Ni NPs were highly crystalline and mainly constituted by Ni metal (**Fig. 1 b**). Diffraction peaks corresponding to NiO, $Ni(OH)_2$ or Ni_2O_3 were undetectable in the diffractogram as can be appreciated in **Fig. 1 b**.

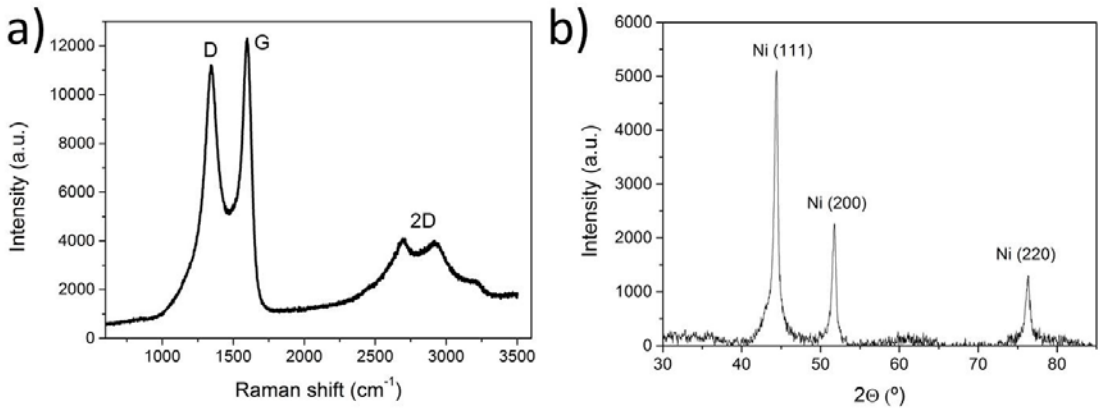

Fig. 1. Raman spectrum of *fl*-G obtained from alginate pyrolysis and subsequent exfoliation recorded upon 512 nm laser excitation (a). XRD pattern of Ni(23)-G photocatalyst (b).

The presence of NiO/Ni NPs on the *fl*-G sheets was observed by HRTEM and confirmed by FESEM, EDS and elemental mapping (**Fig. S2** in supplementary Information). **Fig. 2a** corresponds to a representative HRTEM image of NiO/Ni-G showing that NiO/Ni NPs are homogeneously distributed on *fl*-G sheets. For comparison, an image of *fl*-G sample, prior to Ni deposition, has been also presented as **Fig. 2b** as well as in **Fig. S3** in Supplementary Information. The supported NiO/Ni NPs have a round morphology, as can be observed in the magnified image presented in **Fig. 2c**, with diameters typically smaller than 10 nm, increasing average particle size with the Ni loading on the G sheet. The histogram corresponding to the particle size distribution for the Ni(23)-G is presented in **Fig. 2d**. From the measurement of a statistically relevant number of Ni NPs and average particle size of 8.5 ± 3.5 nm was estimated for this sample in spite of the relatively high Ni loading. High-resolution TEM allowed to measure 0.18 nm for particle lattice fringe that corresponds to the interplanar distance of the 200 facets of fcc Ni metal particles [39], thus, confirming that the particles are mainly constituted by Ni^0.

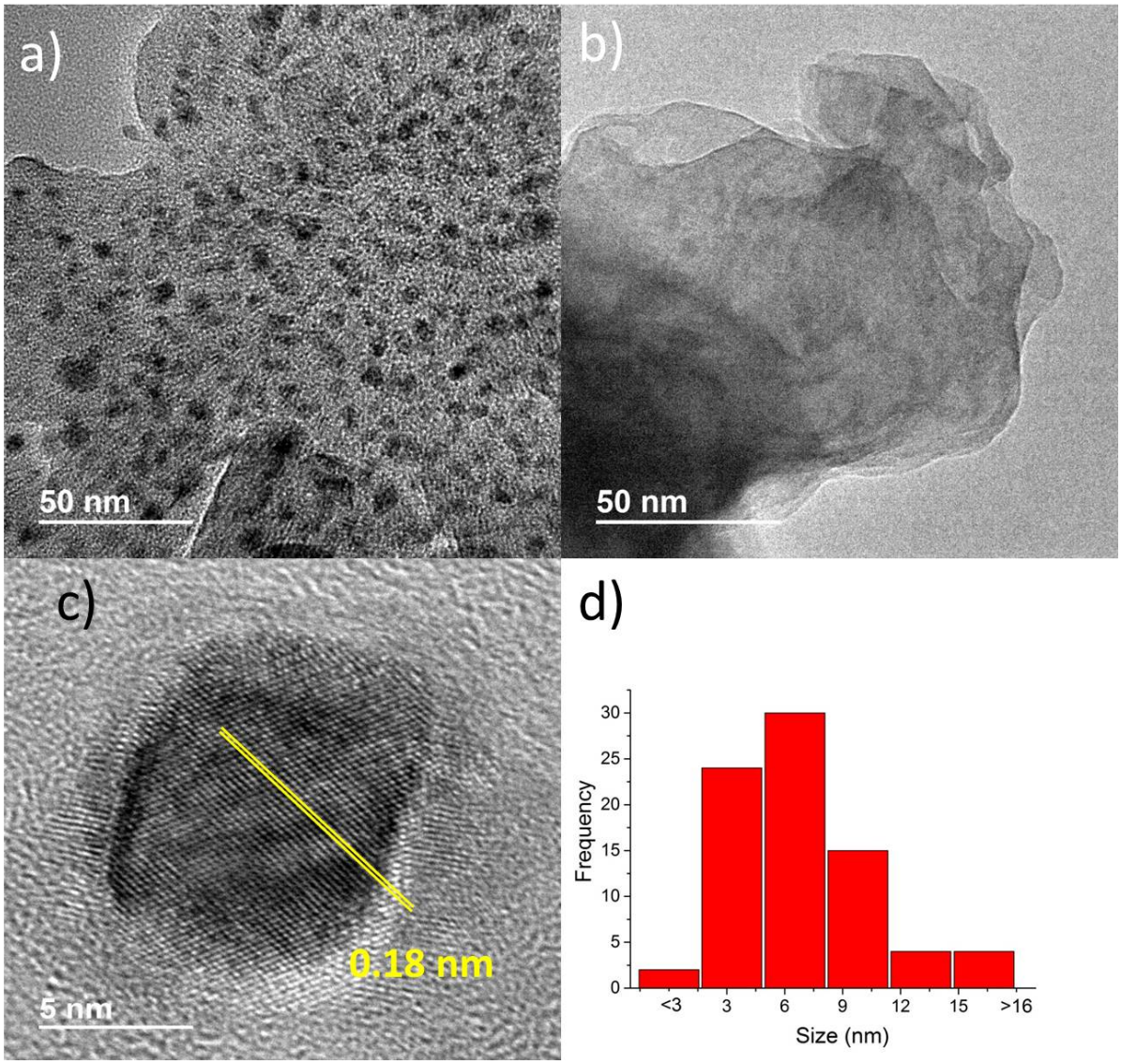

Fig. 2. HRTEM images of Ni(23)-G photocatalyst (a) and *fl*-G (b). Bottom images show a magnification of the main image (a) showing one of the NiO/Ni NP (c) and the particle size distribution (d).

High-resolution XPS peaks of Ni 2p and their corresponding best deconvolution to the different Ni oxidation states are presented in **Fig. 3**. The Ni $2p_{3/2}$ peak shows the presence of two components centered at 853.6 eV and 856.3 eV that can be attributed to Ni^0 and Ni^{II}, respectively. These binding energies are shifted to higher values compared to those reported in the literature for Ni^0 and Ni^{II} at 852 and 854 eV, respectively, indicating the occurrence of charge transfer from NiO/Ni NPs as electron donor to G. Previously, a shift to higher binding energy values of 2 eV was also observed for Ni NPs adsorbed on G [40]. Moreover, in the present case, the Ni^0 is as a minor component of the experimental XPS Ni $2p_{3/2}$ peak. Therefore, in addition to Ni^0 as the predominant phase characterized by XRD, XPS shows the presence of NiO determined by the prominent satellites observed in the Ni $2p_{3/2}$ and Ni $2p_{1/2}$ peaks. To reconcile both observations, it is worth reminding that while XRD probes the whole sample, XPS only provides information of the outermost nanometers of the metal NPs that are more prone to undergo spontaneous oxidation by exposure to the atmosphere. In addition, XRD is useful characterize crystalline NiO and the presence of NiO as amorphous material due to its thin dimensions would be

undetectable by XRD. Therefore, XPS provides two important pieces of information the presence of NiO on the NPs and the charge transfer from NiO/Ni NPs to *fl*-G, implying a notable interaction between them. It should be reminded that even though the preparation of the Ni-G samples was made by H_2 reduction of Ni^{2+}-G at 500 ^{o}C for 2 h, the samples were stored under ambient conditions and this should lead to a fast passivation of the surface of the Ni NPs with the formation of some NiO overlayers.

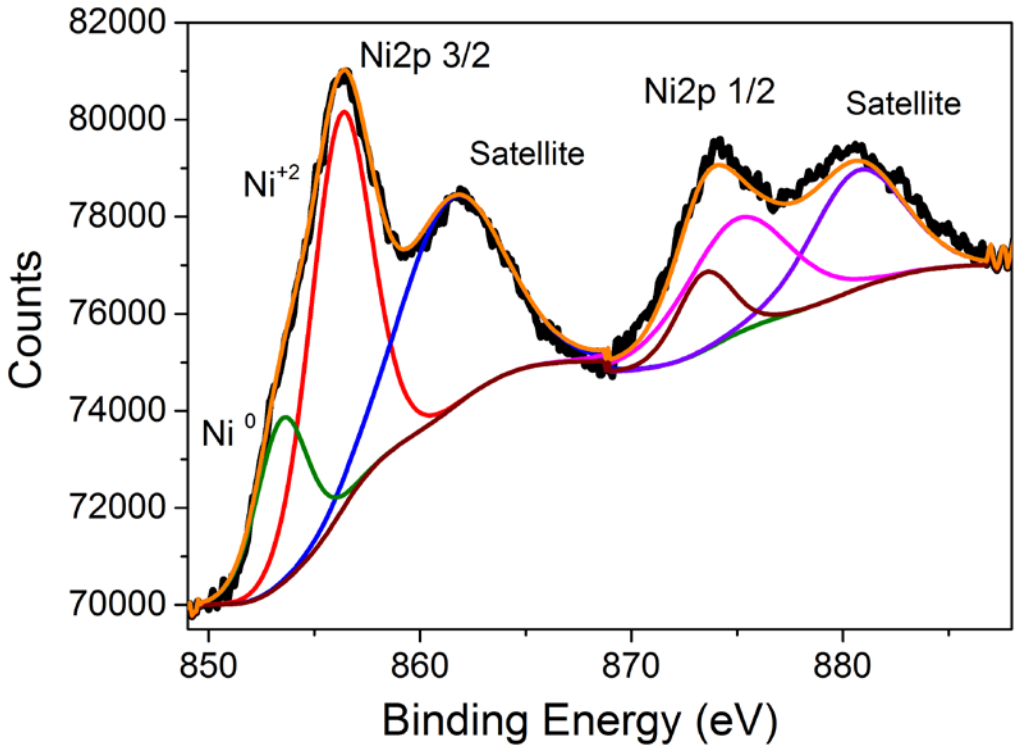

Figure 3. Experimental XPS Ni 2p peaks measured for the Ni(23)-G sample.

The C 1s XPS peak (Supplementary information **Fig. S4**a) shows a major component centered at 284.5 eV corresponding to graphenic sp^2 C, as well as other contributions at 285.5, 286.6 and 289.2 eV corresponding to C atoms bonded to O atoms corresponding to ketones, epoxides and carbonyls groups, respectively. The XPS peak of O 1s (Supplementary Information **Fig. S4b**) can be adequately deconvoluted in two main components corresponding to oxygen atoms bonded to C through single or double bonds. The presence of a component at 529.4 eV corresponding to NiO was also observed, [41] although as a minor component. However, the component at 531.1 eV related to $Ni(OH)_2$ could not be identified, confirming NiO as the main oxide component in the Ni 2p3/2 that should form a thin coating on the major metallic Ni NPs. [41]

The diffuse reflectance UV-Vis spectra of Ni(23)-G and G samples are shown in **Fig. S5**. As can be observed there, the only contribution of the Ni NPs in the NiO/Ni-G photocatalyst absorption is in the UV region, below 350 nm.[42, 43] NiO should present a prominent band centered at 500 nm, however, in the present case this band could not be detected, thus confirming Ni metal as the principal oxidation state in the NPs as indicated by XRD and that the layer of NiO, detectable only by XPS, has to be thin.

2.2. Photocatalytic tests

Photocatalytic tests for CO_2 reduction by H_2 were carried out in a cylindrical quartz reactor equipped with an electrical heating ribbon that allows to heat the reactor at the required temperature. The photocatalyst was placed as a thin millimetric bed on a ceramic crucible under the illuminated reactor area and the photoreactor was charged with 4-to-1 partial pressures of H_2 and CO_2 at a total pressure of 1.3 bar. The temperature of the photoreactor was equilibrated in the dark prior irradiation with UV-Vis light from a 300 W Xe lamp.

Preliminary experiments for the gas phase CO_2 reduction at 200 ^oC and 2236 $W \cdot m^{-2}$ UV-Vis light illumination testing the photo activity of *fl*-G showed that no CH_4 was formed. Then, a series of NiO/Ni-G photocatalysts containing different Ni content were tested under the same conditions for the gas phase CO_2 reduction reaction. The conditions of the experiments and the results achieved are summarized in **Table 1**. All the samples containing NiO/Ni NPs were active to promote photoassisted CH_4 formation. Thus, it can be assumed that NiO/Ni NPs are the component responsible for CH_4 production in accordance with literature precedents [12f]. Therefore, to rank the photo activity of various samples, the specific CH_4 production rates were calculated dividing the mols of CH_4 formed by the mass of Ni and time (μmol $CH_4 \cdot g_{Ni}^{-1} \cdot h^{-1}$). The CH_4 production rate increased with the Ni content up to 23 wt.%, reaching a value of 642 $\mu mol \cdot g_{Ni}^{-1} \cdot h^{-1}$ and a calculated TON per Ni atom of 3.4 were obtained with this optimum load. Considering that CH_4 formation is an eight electrons reduction process, the TON value indicates that each Ni atom is on average involved in 26.2 electron transfer events. Further increase in Ni content produced a detrimental effect in the specific CH_4 production rate, as indicated in Table 1 and can be observed in the **Fig. 4** (inset).

Existence of an optimal Ni loading on G indicates that there should be at least two opposite factors contributing to the observed photocatalytic activity. On one hand, an increase in the Ni loading on *fl*-G should reduce the internal filter effect of light due to defective *fl*-G and favor light absorption by NiO/Ni NPs increasing the activity of the material. In this sense, low percentages of *fl-G* should be more favorable to enhance the photocatalytic activity. On the other hand, upon increase of Ni loading on *fl*-G, an increase in the particle size distribution and a decrease on the percentage of surface Ni atoms (*dispersion*) should occur (compare size of Ni(23)-G and Ni(26)-G in **Table 1** and **Fig. S3** in Supplementary Information), this effect playing a negative role on the photocatalytic activity beyond a certain size. Therefore, higher *fl*-G percentages should favor photocatalytic activity by keeping Ni particle size small and assisting charge separation (*vide infra*), A compromise between these two opposite effects requiring low and high *fl*-G percentage is apparently reached for Ni(23)-G.

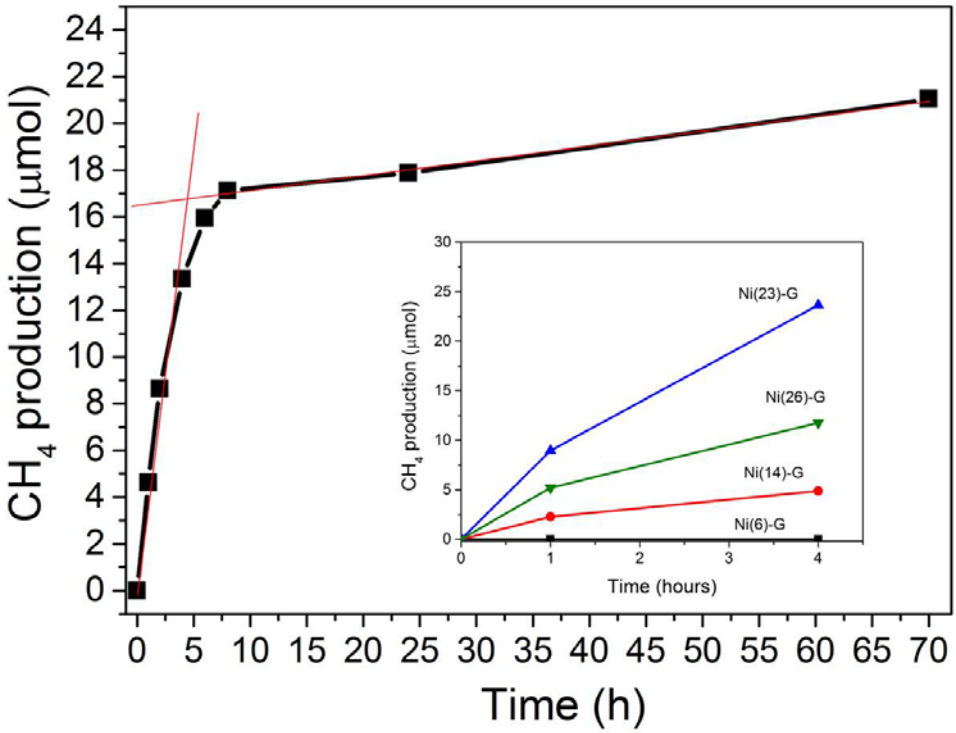

Fig. 4. CH_4 evolution using the Ni(23)-G photocatalyst at 200 ^{o}C and 2236 W·m^{-2} illumination. 34.7 mg of Ni(23)-G and partial pressures of 1.05 and 0.25 bar for H_2 and CO_2, respectively, were used. The inset shows the CH_4 evolution of the NiO/Ni-G photocatalysts with different Ni loading. The amount of the different photocatalysts employed corresponds to those indicated in **Table 1**.

In order to confirm the origin of the C source in the CH_4 production and the formation of H_2O according to **Equation 1** $^{13}C^{18}O_2$ was used as substrate and the obtained products were analyzed after 2 h reaction under optimal conditions by GC-MS spectroscopy (**Fig. S6** in Supplementary Information). The analysis shows a mix of 14% of unlabeled $^{12}CH_4$ and 86 % of $^{13}CH_4$, indicating that a minor portion of the produced CH_4 does not come from the labelled substrate. The most likely origin of the unlabeled CH_4 should be the C atoms of *fl*-G. In order to confirm this hypothesis a stability experiment was performed submitting Ni(23)-G sample at reaction conditions (200 ^{o}C and 2236 W·m^{-2}) under Ar atmosphere, and measuring the CO_2 evolution (**Fig. S7** in Supplementary Information). As can be observed a small amount of CO_2 was observed to evolve under these conditions for the first 20 h. After this period, the CO_2 amount remained constant, confirming, on the one hand, the presence of small amounts of CO_2 originated from *fl*-G and, on the other hand, that the photocatalyst is photostable at long reaction times. It should be, however, reminded that the blank experiment with *fl*-G in where formation of CH_4 was not observed, indicates that even for this contribution of unlabeled CH_4, the presence of NiO/Ni is needed. In the same experiment using $^{13}C^{18}O_2$, observation of $H_2{}^{18}O$ was also detected (see **Fig. S6**), confirming the formation of H_2O in the methanation.

$$CO_2 + 4\,H_2 \rightarrow CH_4 + 2\,H_2O \qquad \Delta G = -\,115\ KJ\cdot mol^{-1} \qquad \textbf{(Equation 1)}$$

Control experiments also confirmed that heating and light are necessary to produce CH_4 under the present experimental conditions, since CO_2 does not undergo reduction by Ni(23)-G upon irradiation at room temperature or in the dark at 200 ^oC by covering the photoreactor with aluminum foil with the light on (see data in **Table 1**). A different control experiment was carried out where Ni(23)-G sample was submitted to H_2 atmosphere at 200 ^oC for 4 prior utilization as photocatalysts in methanation reaction under light irradiation at room temperature (**Table 1**), however, evolution CH_4 was no detected, indicating that temperature is playing a different role to photocatalyst activation as it will be discussed bellow. The results of the above control experiments are in good agreement with prior studies in the area that have shown that other Ni materials can promote the photoassisted CO_2 reduction by H_2, in particular Ni-Al_2O_3 and NiO.[44-46]

To put the photocatalytic activity of Ni(23)-G into context, additional experiments were carried out with commercial samples of Ni-Al_2O_3/SiO_2 and NiO NPs (< 50 nm) from Aldrich that have been reported previously as photocatalysts for CO_2 methanation.[46] The photocatalytic activity of Ni-Al_2O_3/SiO_2 and NiO NPs was evaluated in the same photoreactor under identical conditions as those used for Ni(23)-G. The results are included also in **Table 1**. As can be seen there, using similar amounts of Ni, the specific CH_4 production rate of Ni-Al_2O_3/SiO_2 was about half that of the Ni(23)-G, suggesting that *fl*-G is not only acting as support of the Ni NPs, but also is contributing to the photoassisted process, probably favoring charge separation as it will be commented below when discussing the reaction mechanism. Moreover, the use of NiO NPs resulted in one order of magnitude lower rate, indicating that metal Ni NPs with the overlayer of spontaneously formed NiO are more active in this reaction than NiO using identical conditions. On the other hand, the commercial NiO NPs were supported in *fl*-G by impregnation (see STEM image in **Fig. S8** in supplementary information), and their photocatalytic activity tested under identical conditions as those used for Ni(23)-G. As can be seen in **Table 1,** a CH_4 production of 69.86 $\mu mol \cdot g^{-1} \cdot h^{-1}$ was obtained. This is indicating that the strong interaction between the *fl*-G and the NiO/Ni NPs of Ni-G samples, obtained by the experimental procedure reported here, and/or the NiO/Ni heterojunction confer about one order magnitude higher CH_4 production than supporting preformed NiO NPs directly on *fl*-G.

The temporal CH_4 evolution using the Ni(23)-G sample as photocatalyst at 200 ^oC and 2236 $W \cdot cm^{-2}$ irradiation is shown in **Fig. 4**. As can be seen there, the initial CH_4 production was constant only during 4 h. However, after 4 h, the CH_4 production rate decreased. Linear fits of the experimental points at the beginning of the reaction (4 h) and at long reaction times (from 8 to 70 h) are depicted in **Fig. 4** as red lines. As can be seen, two different slopes can be clearly identified. At initial reaction times a fast CH_4 evolution can be observed, while at longer times the slope becomes smaller, although still constant for 70 h reaction. XPS measurements after recovery of the used Ni(23)-G sample from the photoreactor and exposure to the ambient revealed that the Ni 2p 3/2 spectrum after reaction (Supplementary Information **Fig. S9**) was very similar to the XPS presented in **Fig. 3**, indicating that the oxidation state of the outermost part of the Ni NPs probed by XPS is not modified by the reaction conditions. In contrast, TEM images of the Ni(23)-G photocatalyst after reaction revealed an increase in the Ni NP size distribution (**Fig. S10**). The average particle size of the photocatalysts after reaction was determined as 19.3 ± 9.7 nm, significantly higher than 8.5 ± 3.5 nm measured for the fresh sample. This particle size growth is a general observation when metal NPs are submitted to heating at temperatures about 200 ^oC for prolonged periods. As indicated previously when justifying the influence of Ni loading on G on the photocatalytic activity, large particle sizes such as that of Ni(26)-G (13.7±6 nm) are detrimental for the photocatalytic activity, reducing approximately to the half the CH_4 production rate, due to the lower

proportion of exposed active metals at the surface. Therefore, the sintering process that the NiO/Ni NPs suffer under the reaction conditions at the initial reaction stage should be responsible for a decrease in the rate of CH_4 production, although then the rate becomes constant at least for 70 h.

3.3. Mechanism.

Although no changes in the XP spectrum of Ni(23)-G before and after the reaction could be observed, we were interested in ascertain the presence of NiO under the reaction conditions, particularly considering the reductive conditions and the temperature of the methanation. Aimed at this purpose, the experimental XPS analysis of Ni(23)-G prior reaction was compared to that measured *in situ* under the reaction conditions. Thus, a Ni(23)-G sample was submitted to H_2 atmosphere at 200 ^oC for 4 h, measuring *in situ* the Ni 2p peak in the XPS spectrum without exposure to the ambient (**Fig. S11**). As can be observed, the component related to Ni^0 (around 853 eV) becomes higher under the reaction conditions compared to the sample prior to the reaction. However, the XPS component corresponding to NiO is still bigger than that of the Ni metal. In fact, the relative percentage of Ni^0 in the sample before and under *in situ* conditions changed from 15 % to 23.5%, respectively. These measurements clearly confirm that in spite of the reductive conditions, the thin layer of NiO should be still present, particularly at initial reaction times that is when the NiO/Ni-G photocatalyst exhibits the highest photocatalytic activity. It can be, therefore, suggested that it is in this outermost part of NiO in contact with Ni where the reaction takes place.

To gain further information on the reaction mechanism and the role of Ni in the process, Ni(23)-G was placed in a sealed reactor and exposed to a H_2 atmosphere at 200 ^oC for 4 h and then, the sample was allowed to cool down under Ar flow ensuring the complete removal of H_2 gas. Subsequently, the reactor was load only with CO_2 and submitted to the general reaction conditions at 200 ^oC and 2236 $W \cdot m^{-2}$ illumination. After 18 h reaction, a detectable amount of CH_4 was measured, suggesting the formation of Ni-H species in the first step, without the need of photoactivation that subsequently are able to promote photoassisted CO_2 reduction as reported before [46].

As commented above, the photoassisted CO_2 reduction by NiO/Ni-G requires the combination of heating and irradiation to occur. The influence of light intensity and temperature on the photocatalytic CO_2 reduction reaction using Ni(23)-G was, therefore, studied to establish this dependency. The results are presented in **Fig. 5**.

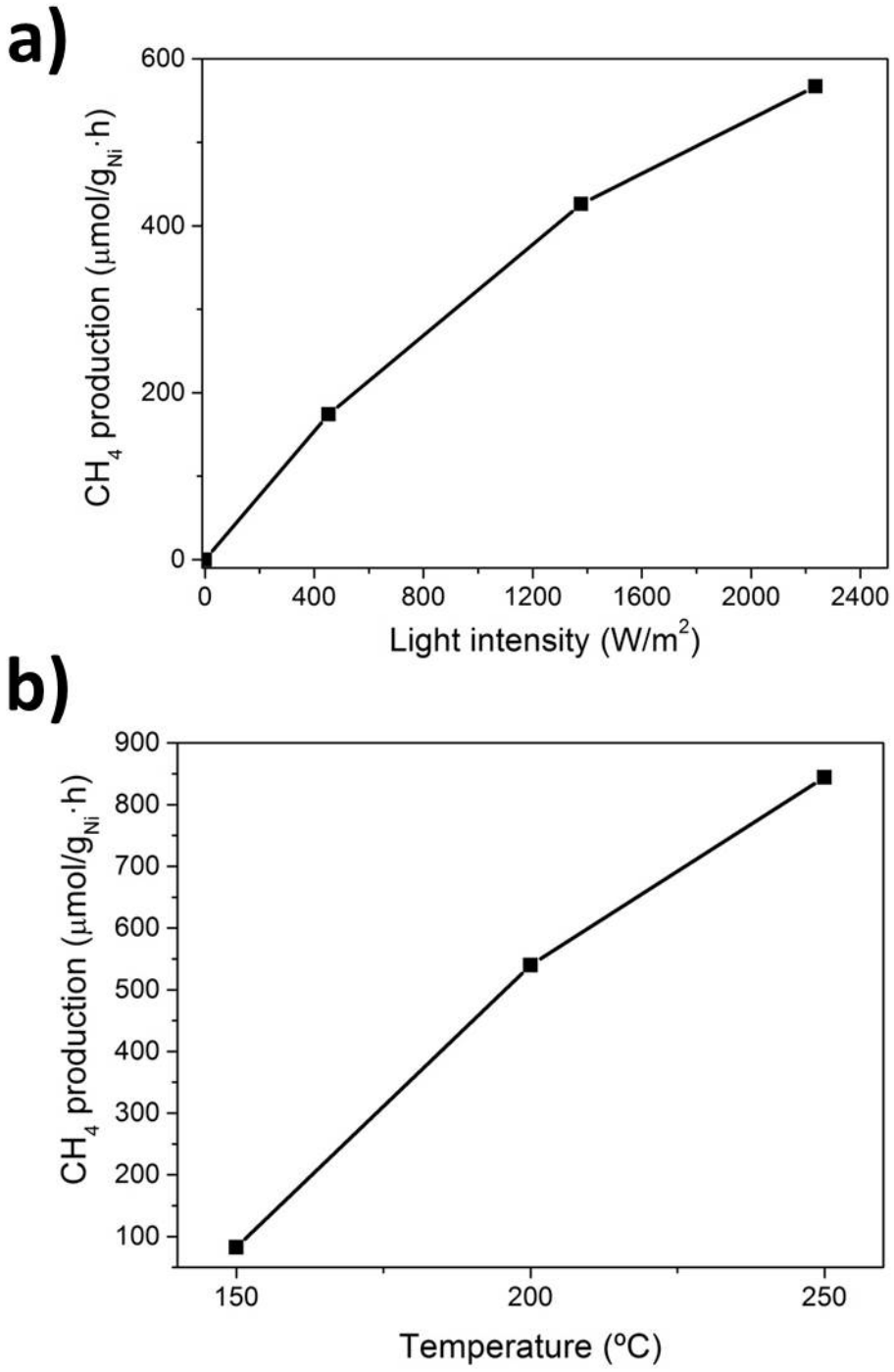

Figure 5. Specific CH_4 production rate of Ni(23)-G photocatalyst as a function of the light intensity (a) and temperature (b). The total catalyst amount employed in the light intensity and temperature experiments was of 25 and 36 mg, respectively. Light intensity tests were performed at a constant temperature of 200 ^{o}C, while the light intensity in the temperature dependency experiments was of 2236 W·m^{-2}. P_{H2} = 1.05 bar, P_{CO2} = 0.25 bar in all cases.

As can be observed in **Fig. 5**, the specific CH_4 production initial rate is clearly dependent of the irradiation power, confirming that, under the present conditions, the CO_2 methanation is a photoassisted process. The apparent quantum yield at 200 ^{o}C in the photocatalytic CO_2 reduction using the Ni(23)-G

photocatalyst was estimated of 1.98 %. On the other hand, the specific CH_4 production initial rate at constant illumination varied also as a function of the reaction temperature. As commented before, reactions performed at room temperature resulted in negligible CH_4 production initial rate (see last entry in Table 1 and footnote f). Heating the photoreactor at 150 ^oC resulted in CH_4 evolution rates below 100 $\mu mol \cdot g_{Ni}^{-1} \cdot h^{-1}$. However, temperature of 250 ^oC produced CH_4 at a specific rate of 850 $\mu mol \cdot g_{Ni}^{-1} \cdot h^{-1}$, approximately. The dependency of the specific CH_4 production rate with the temperature of the system allows us to calculate an apparent activation energy of 38.6 $kJ \cdot mol^{-1}$ for the process.

To gain understanding on the mechanism of the photoassisted CO_2 methanation promoted by NiO/Ni-G as photocatalyst and, particularly, the possible role of photogenerated electrons and holes, a series of experiments adding probe molecules were performed. Specifically, a series of photocatalytic tests were carried out adding compounds with increasing ability to act as electron donors. It was assumed that if the mechanism of the photoassisted reaction involves charge separation, the presence of additives that could act as sacrificial electron donor or acceptor agents should enhance or stop, respectively, the photocatalytic activity. Ideally the presence of these electron donor/acceptor additives should not influence the thermal methanation mechanism, at least, in a large extent.

Therefore, the photoassisted CO_2 reduction using Ni(23)-G as promoter was carried out in the presence of dimethylaniline, anisole and p-xylene as electron donors (oxidation potentials of 0.9, 1.92 and 2.17 V vs. Ag/AgCl, respectively) and 4-nitrobenzene as electron acceptor quenchers. Note that according to their boiling points the sacrificial agents are in all cases in the gas phase at the reaction temperature. It was observed that the presence of *N*,*N*-dimethylaniline (0.16 mmol) increases the specific CO_2 reduction initial rate by a factor over 2.5, reaching a value of 1600 $\mu mol \cdot g_{Ni}^{-1} \cdot h^{-1}$. CH_4 was also formed in the presence of anisole as electron donor, although at much slower initial reaction rate than in the case of *N*,*N*-dimethylaniline in accordance with its higher oxidation potential. In contrast, the presence of p-xylene (oxidation potential of 2.17 V vs. Ag/AgCl) completely stopped the production of CH_4, since this aromatic molecule would not be able to quench the holes on Ni(23)-G due to its high oxidation potential (see **Fig. 6**). In the presence of nitrobenzene acting as electron acceptor quencher, CO_2 reduction was also quenched, due to the preferential trapping of electrons by nitrobenzene that has a lower reduction potential compared to CO_2. Note that it would be hard to explain any influence of the presence of electron donor/acceptor quenchers at this small concentration if a photothermal mechanism were operating.

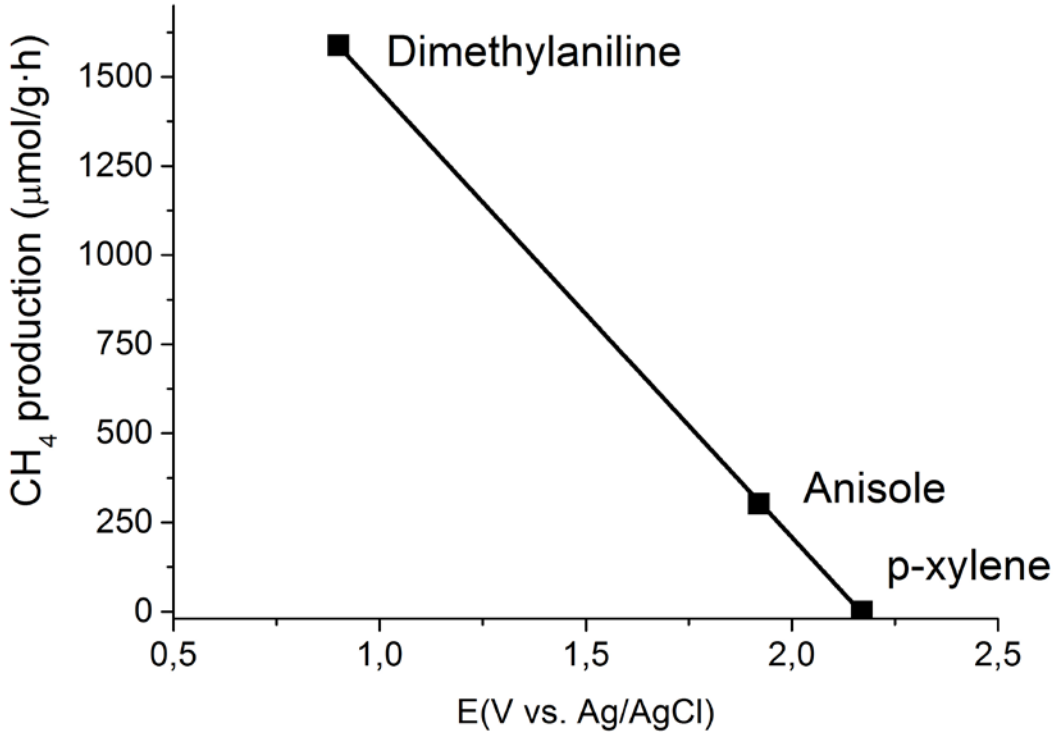

Figure 6. CH_4 production as function of the sacrificial agent oxidation potential. The CH_4 production rate was measured at 1 h under constant light intensity of 2236 $W \cdot m^{-2}$ from a 300 W Xenon lamp at 200 ^oC. P_{H2} = 1.05 bar, P_{CO2} bar. 20 µL of each sacrificial agent was added to the reactor vessel in each experiment.

Photogeneration of charges and its role in CO_2 reduction by NiO/Ni-G was also in agreement with the photoresponse spectrum. It was observed that the photocatalytic activity of NiO/Ni-G is due exclusively to the UV light and that filtering UV region (< 350 nm) and irradiating exclusively with visible light leads to the complete disappearance of the photocatalytic activity. This behavior is in agreement with the absorption spectrum of NiO/Ni-G that, as previously commented, exhibits an electronic absorption band in the UV region with onset about 360 nm (**Fig. S5**). This absorption on the UV region indicates that NiO (bandgap 2.83 eV) is present on the NiO/Ni-G as a minor component and with absorption by graphene being not responsible for the photocatalysis. It is frequently observed that photothermal effects in which light is converted into heat by the metal NPs occurs upon irradiation in the visible and even in the NIR regions [47]. In contrast, photoinduced charge separation requires electronic excitation between two energy levels, leading to the generation of electrons and holes and this process is often observed only with UV light.

Transient absorption measurements were carried out to provide support to the generation of charge separation due to the interaction of NiO/Ni NPs and *fl*-G. Aimed at this purpose, an Ar-purged *fl*-G dispersion in acetonitrile (1 $mg \cdot mL^{-1}$) was submitted to 355 nm laser pulse excitation and the transient spectrum was acquired at 30 ns (**Fig. 7a**). As can be observed in **Fig. 7** the transient spectrum of the *fl*-G dispersion corresponds to a continuous band decreasing in intensity towards the red part of the spectrum [48]. This behavior has been observed previously in similar graphenic materials and attributed to the

charge separation state decaying in microsecond time scale [48]. In a second control, commercial NiO NPs (< 50 nm) from Aldrich were partially reduced in an aqueous N_2H_2 solution (50% vol) to NiO/Ni as determined by XRD in order to simulate the NiO/Ni NPs that are present on the NiO/Ni-G samples, Then, the partially reduced NiO/Ni NPs were dispersed in acetonitrile (1 mg·mL^{-1}) and the transient spectrum was also acquired upon 355 nm laser excitation (**Fig. 7a**). A negative signal corresponding to the bleaching of NiO/Ni ground state absorption was observed. Finally, a small aliquot of the dispersed NiO/Ni NPs corresponding to 0.5 mg was added to the *fl*-G suspension (2 mg) in acetonitrile and the transient spectrum recorded at 30 ns upon 355 nm laser excitation (**Fig. 7a**). It was observed that addition of NiO/Ni NPs induces quenching of the signal observed for the *fl*-G dispersion, supporting the interaction of the charge separation state of *fl*-G flakes and the NiO/Ni NPs.

The transient signals of the *fl*-G, NiO/Ni NPs and *fl*-G containing Ni NPs were monitored at different wavelengths, obtaining for all the wavelength identical results. **Fig. 7b** shows the kinetics of the transient signal decay of the three samples monitored at 415 nm. As can be observed, the sample containing *fl*-G presents a transient decay that can be fitted to a single exponential with a lifetime of 36 ns. The transient decay of the NiO/Ni NPs dispersion is presented in **Fig. S12**, and presents bi-exponential kinetics with a fast (τ_1=115 ns) and a slow (τ_1=3414 ns) component. When NiO/Ni NPs were added to the *fl*-G suspension the transient kinetics become faster, determining a lifetime of 26 ns from the single exponential fitting to the experimental points. Quenching of photoinduced *fl*-G charge separation state by NiO/Ni could lead to a new transient with electrons and holes located in the different components. The fact that growth of a new signal as result of the quenching is not observed could be due to a weak absorption of these transients. Overall, transient absorption spectroscopy provides evidence of the interaction of photoinduced charge separation state of *fl*-G and the NiO/Ni NPs. This interaction of the charge separate state should equally occur in Ni-G samples in good agreement with the previous experiments with sacrificial electron donors and acceptors. Therefore, the role of graphene in Ni-G systems will be to assist charge separation with migration of electrons from NiO/Ni to the graphene sheet. This more favorable charge separation would be responsible for the higher photocatalytic activity of Ni-G respect to commercial NiO and related NiO/Ni and even than that of Ni-Al_2O_3/SiO_2, where electron delocalization of the inorganic metal oxide support is not possible.

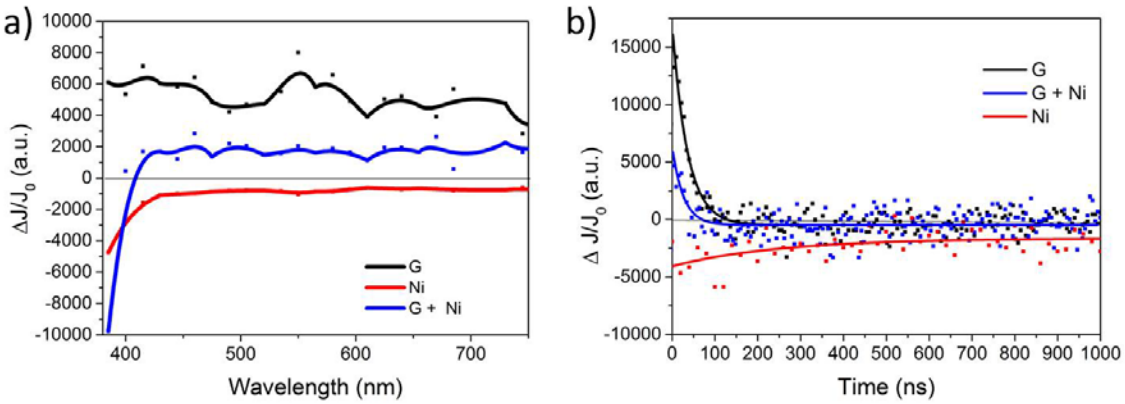

Figure 7. Transient spectra (a) and kinetics (b) of Ar-purged *fl*-G (black), NiO/Ni NPs (red) and fl-G with Ni NPs (blue) suspensions. Laser excitation 355 nm. Acquisition time for *fl*-G and *fl*-G with Ni NPS was 30 ns, and 500 ns for NiO/Ni NPs sample. Transient kinetics monitored at 415 nm.

On the other hand, to understand the role of the temperature on the photocatalytic process, a series of experiments adding to the reaction vessel small aliquots of H_2O, in the range of the amounts that should be formed in the methanation, were carried out (**Fig. 8**). It was reasoned that the value of the activation energy determined from the Arrhenius plot of the logarithm of the relative initial reaction rates with the inverse of the absolute temperature is relatively low for a transition state involving bond cleavage, while this value of activation energy is more common for the heat of H_2O desorption from the photocatalyst surface. It should be noted that $H_2{}^{18}O$ formation was detected in the $^{13}C^{18}O_2$ labelled experiments. According to the stoichiometry (**Equation 1**), methanation of CO_2 should also produce two H_2O molecules and that at low temperatures these molecules could be preferentially adsorbed on the surface of the photocatalyst, resulting in the inhibition of the reaction.

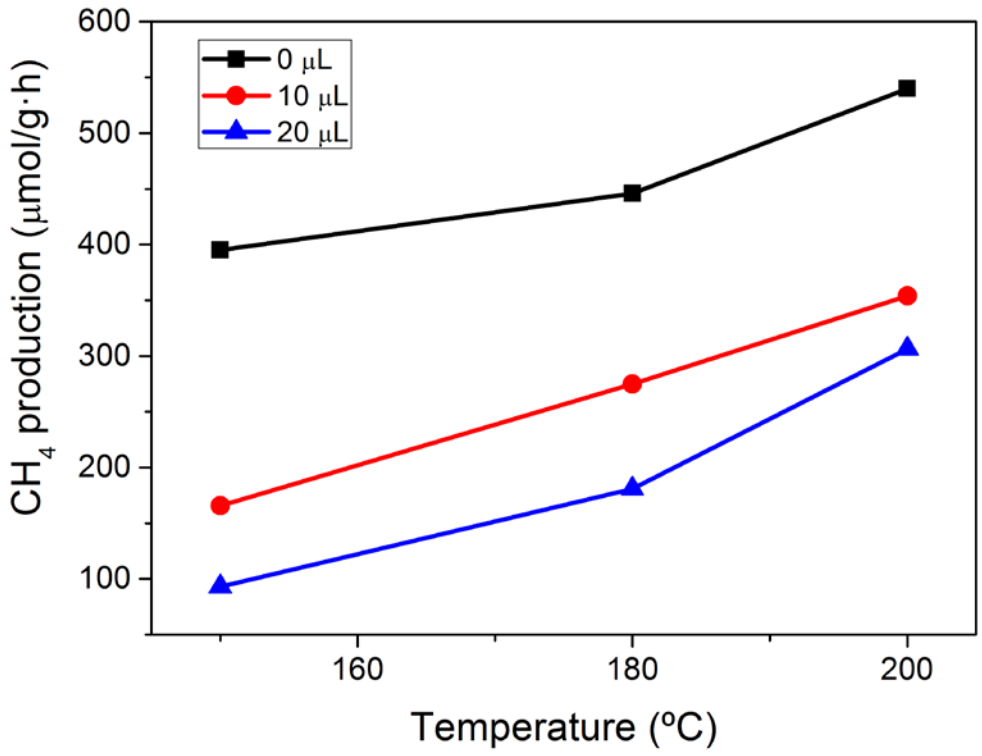

Figure 8. Specific CH_4 production rate measured at different reaction temperatures without (a) or upon addition of 10 µL (b) and 20 µL (c) of H_2O. Reaction conditions: 2236 $W \cdot m^{-2}$, 25 mg of Ni(23)-G catalyst and P_{H2} = 1.05 bar, P_{CO2} bar in all experiments.

As can be observed in **Fig. 8**, addition of 10 or 20 µL of H_2O in the reaction media resulted in a detrimental effect on the specific CH_4 production rate, proportional to the amount of H_2O, the higher the amount of H_2O present at any of the temperatures studied, the lower the specific CH_4 production rate. Therefore, it is proposed that a possible role of the temperature in the system could be to favor H_2O desorption from the photocatalysts surface, giving an opportunity for H_2 and CO_2 activation. Note that according to the data presented in **Fig. 4** and the stoichiometry of the reaction, the amount of H_2O formed at final reaction times should correspond to the addition of about 890 µl and that the amount of H_2O tested in **Fig. 8** is similar to the amount formed at the early stages of methanation. Even with these

relatively low H_2O concentrations, their negative influence is already clearly observed in **Fig. 8**. Therefore, it is clear that H_2O is a strong poison of the photomethanation and, it is proposed that the role of the temperature is to desorb this generated H_2O acting as poison from the catalyst surface.

Finally, the photocatalytic activity of the NiO/Ni-G catalyst was evaluated under continuous flow operation. Continuous flow is very convenient to test photocatalyst stability and the influence of the contact time on the conversion. In the present study, a total flow of 14.79 $mL \cdot min^{-1}$ containing a 76.8 % of N_2, 18.8 % of H_2 and 4.4 % of CO_2 was passed through a cylindrical quartz reactor containing 50.7 mg of the Ni(23)-G photocatalyst loaded on the top of a fritted glass filter inside the reactor. Considering the volume of the photocatalyst (0.75 ml) and the gas flow, the contact time of CO_2 with the irradiated catalysts was 3.1 s. The cylindrical photoreactor was heated at 200 ^oC by means of an electrical heating ribbon controlled with a thermocouple and the irradiation was carried out using the same light source used in the previous experiments, but the light intensity at the photocatalyst was 754.7 $W \cdot m^{-2}$. A photograph of the system is provided in the Supplementary Information (**Fig. S13**).

The temporal evolution of the continuous flow CH_4 formation was followed for 4 h, obtaining a maximal specific CH_4 formation rate of 4.74 $\mu L \cdot min^{-1}$ that was decaying gradually up to 4.08 $\mu L \cdot min^{-1}$, indicating the occurrence of a certain deactivation. The specific CH_4 production rate of the continuous flow was compared with those of the production rate under batch conditions (**Fig. S14**). It can be observed that the loss in CH_4 production rate in the batch reaction was of 28 % during for 4 h. However, in continuous flow this activity decay was of 86 % for the same period of time. This indicates that the conditions of the continuous flow are more favorable for the stability of Ni(23)-G photocatalyst. It is proposed that this higher stability of Ni(23)-G photocatalyst under continuous flow derives from the more favorable removal of H_2O from the photocatalyst by the gas flow as this by-product is being formed in the reaction. Moreover, the estimated quantum yield for the continuous flow experiments was 0.86 %.

4. Conclusions

There is a considerable interest in increasing the photocatalytic activity of conventional semiconductors and it has been shown that graphene can be a suitable additive that can contribute to enhance the photocatalytic activity [32]. In the present manuscript it has been shown that NiO/Ni NPs supported on *fl*-G is a suitable photocatalyst to perform methanation of CO_2 at temperatures about 200 ^oC, reaching specific CH_4 formation rates of 642 $\mu mol \cdot g_{Ni}^{-1} \cdot h^{-1}$ that are about double than that measured for Ni NPs supported on high surface area silica-alumina and apparent quantum yields of 1.98 %. The positive effect of graphene appears to be due to the photoinduced electron transfer from excited NiO/Ni NPs to the graphene sheet. Experimental evidence indicates that the role of the temperature is to desorb H_2O formed also in the process, causing apparent deactivation of the photocatalyst. Under optimal conditions under continuous flow, photocatalyst deactivation was reduced probably to the more favorable H_2O removal. Mechanistic data using electron donor and acceptor quenchers and observation of *fl*-G charge separated stated quenching by NiO/Ni NPs support that the reaction mechanism involves photogenerated charge separation derived from photon absorption in the UV region.

Acknowledgments

Financial support by the Spanish Ministry of Economy and Competitiveness (Severo Ochoa SEV-2016-0683, Grapas and CTQ2015-69563-CO2-R1) and by the Generalitat Valencia (Prometeo 2013-014) is gratefully acknowledged. J. A. thanks the Universitat Politècnica de València for a

postdoctoral scholarship. D. M. also thanks Spanish Ministry of Science for PhD Scholarship.

References:

[1] J.A. Herron, J. Kim, A.A. Upadhye, G.W. Huber, C.T. Maravelias, A general framework for the assessment of solar fuel technologies, Energy & Environmental Science, 8 (2015) 126-157.

[2] J.A. Herron, C.T. Maravelias, Assessment of Solar-to-Fuels Strategies: Photocatalysis and Electrocatalytic Reduction, Energy Technology, 4 (2016) 1369-1391.

[3] J. Kim, T.A. Johnson, J.E. Miller, E.B. Stechel, C.T. Maravelias, Fuel production from CO2 using solar-thermal energy: system level analysis, Energy & Environmental Science, 5 (2012) 8417-8429.

[4] N.S. Lewis, D.G. Nocera, Powering the planet: Chemical challenges in solar energy utilization, Proceedings of the National Academy of Sciences of the United States of America, 103 (2006) 15729-15735.

[5] A. Corma, H. Garcia, Photocatalytic reduction of CO2 for fuel production: Possibilities and challenges, Journal of Catalysis, 308 (2013) 168-175.

[6] A. Dhakshinamoorthy, S. Navalon, A. Corma, H. Garcia, Photocatalytic CO2 reduction by TiO2 and related titanium containing solids, Energy & Environmental Science, 5 (2012) 9217-9233.

[7] J. Barber, Photosynthetic energy conversion: natural and artificial, Chemical Society Reviews, 38 (2009) 185-196.

[8] D. Gust, T.A. Moore, A.L. Moore, Solar Fuels via Artificial Photosynthesis, Accounts of Chemical Research, 42 (2009) 1890-1898.

[9] M.-Q. Yang, N. Zhang, M. Pagliaro, Y.-J. Xu, Artificial photosynthesis over graphene-semiconductor composites. Are we getting better?, Chemical Society Reviews, 43 (2014) 8240-8254.

[10] W. Fan, Q. Zhang, Y. Wang, Semiconductor-based nanocomposites for photocatalytic H-2 production and CO2 conversion, Physical Chemistry Chemical Physics, 15 (2013) 2632-2649.

[11] E.V. Kondratenko, G. Mul, J. Baltrusaitis, G.O. Larrazabal, J. Perez-Ramirez, Status and perspectives of CO2 conversion into fuels and chemicals by catalytic, photocatalytic and electrocatalytic processes, Energy & Environmental Science, 6 (2013) 3112-3135.

[12] W. Tu, Y. Zhou, Z. Zou, Photocatalytic Conversion of CO2 into Renewable Hydrocarbon Fuels: State-of-the-Art Accomplishment, Challenges, and Prospects, Advanced Materials, 26 (2014) 4607-4626.

[13] H. Huang, J. Lin, G. Zhu, Y. Weng, X. Wang, X. Fu, J. Long, A Long-Lived Mononuclear Cyclopentadienyl Ruthenium Complex Grafted onto Anatase TiO2 for Efficient CO2 Photoreduction, Angewandte Chemie International Edition, 55 (2016) 8314-8318.

[14] M. Tahir, B. Tahir, N.A. Saidina Amin, H. Alias, Selective photocatalytic reduction of CO2 by H2O/H2 to CH4 and CH3OH over Cu-promoted In2O3/TiO2 nanocatalyst, Applied Surface Science, 389 (2016) 46-55.

[15] M. Li, P. Li, K. Chang, T. Wang, L. Liu, Q. Kang, S. Ouyang, J. Ye, Highly efficient and stable photocatalytic reduction of CO2 to CH4 over Ru loaded NaTaO3, Chemical Communications, 51 (2015) 7645-7648.

[16] X. Meng, T. Wang, L. Liu, S. Ouyang, P. Li, H. Hu, T. Kako, H. Iwai, A. Tanaka, J. Ye, Photothermal Conversion of CO2 into CH4 with H-2 over Group VIII Nanocatalysts: An Alternative Approach for Solar Fuel Production, Angewandte Chemie-International Edition, 53 (2014) 11478-11482.

[17] J. Ren, S. Ouyang, H. Xu, X. Meng, T. Wang, D. Wang, J. Ye, Targeting Activation of CO2 and H-2 over Ru-Loaded Ultrathin Layered Double Hydroxides to Achieve Efficient Photothermal CO2 Methanation in Flow-Type System, Advanced Energy Materials, 7 (2017).

[18] K.K. Ghuman, L.B. Hoch, P. Szymanski, J.Y.Y. Loh, N.P. Kherani, M.A. E-Sayed, G.A. Ozin, C.V. Singh,

Photoexcited Surface Frustrated Lewis Pairs for Heterogeneous Photocatalytic CO2 Reduction, Journal of the American Chemical Society, 138 (2016) 1206-1214.
[19] J. Jia, P.G. O'Brien, L. He, Q. Qiao, T. Fei, L.M. Reyes, T.E. Burrow, Y. Dong, K. Liao, M. Varela, S.J. Pennycook, M. Hmadeh, A.S. Helmy, N.P. Kherani, D.D. Perovic, G.A. Ozin, Visible and Near-Infrared Photothermal Catalyzed Hydrogenation of Gaseous CO2 over Nanostructured Pd@Nb2O5, Advanced Science, 3 (2016).
[20] P.G. O'Brien, A. Sandhel, T.E. Wood, A.A. Jelle, L.B. Hoch, D.D. Perovic, C.A. Mims, G.A. Ozin, Photomethanation of Gaseous CO2 over Ru/Silicon Nanowire Catalysts with Visible and Near-Infrared Photons, Advanced Science, 1 (2014).
[21] R. Schloegl, The Revolution Continues: Energiewende 2.0, Angewandte Chemie-International Edition, 54 (2015) 4436-4439.
[22] G. Du, S. Lim, Y. Yang, C. Wang, L. Pfefferle, G.L. Haller, Methanation of carbon dioxide on Ni-incorporated MCM-41 catalysts: The influence of catalyst pretreatment and study of steady-state reaction, Journal of Catalysis, 249 (2007) 370-379.
[23] T. Inui, M. Funabiki, M. Suehiro, T. Sezume, METHANATION OF CO2 AND CO ON SUPPORTED NICKEL-BASED COMPOSITE CATALYSTS, Journal of the Chemical Society-Faraday Transactions I, 75 (1979) 787-802.
[24] Y.-x. Pan, C.-j. Liu, Q. Ge, Effect of surface hydroxyls on selective CO2 hydrogenation over Ni-4/gamma-Al2O3: A density functional theory study, Journal of Catalysis, 272 (2010) 227-234.
[25] S. Abello, C. Berrueco, D. Montane, High-loaded nickel-alumina catalyst for direct CO2 hydrogenation into synthetic natural gas (SNG), Fuel, 113 (2013) 598-609.
[26] P. Frontera, A. Macario, M. Ferraro, P. Antonucci, Supported Catalysts for CO2 Methanation: A Review, Catalysts, 7 (2017).
[27] C.N.R. Rao, A.K. Sood, K.S. Subrahmanyam, A. Govindaraj, Graphene: The New Two-Dimensional Nanomaterial, Angewandte Chemie International Edition, 48 (2009) 7752-7777.
[28] D. Mateo, I. Esteve-Adell, J. Albero, A. Primo, H. García, Oriented 2.0.0 Cu2O nanoplatelets supported on few-layers graphene as efficient visible light photocatalyst for overall water splitting, Applied Catalysis B: Environmental, 201 (2017) 582-590.
[29] R. Gusain, P. Kumar, O.P. Sharma, S.L. Jain, O.P. Khatri, Reduced graphene oxide–CuO nanocomposites for photocatalytic conversion of CO2 into methanol under visible light irradiation, Applied Catalysis B: Environmental, 181 (2016) 352-362.
[30] P. Kumar, C. Joshi, A. Barras, B. Sieber, A. Addad, L. Boussekey, S. Szunerits, R. Boukherroub, S.L. Jain, Core–shell structured reduced graphene oxide wrapped magnetically separable rGO@CuZnO@Fe3O4 microspheres as superior photocatalyst for CO2 reduction under visible light, Applied Catalysis B: Environmental, 205 (2017) 654-665.
[31] K. Wang, Q. Li, B. Liu, B. Cheng, W. Ho, J. Yu, Sulfur-doped g-C3N4 with enhanced photocatalytic CO2-reduction performance, Applied Catalysis B: Environmental, 176 (2015) 44-52.
[32] J. Low, J. Yu, W. Ho, Graphene-Based Photocatalysts for CO2 Reduction to Solar Fuel, The Journal of Physical Chemistry Letters, 6 (2015) 4244-4251.
[33] A. Nikokavoura, C. Trapalis, Alternative photocatalysts to TiO2 for the photocatalytic reduction of CO2, Applied Surface Science, 391 (2017) 149-174.
[34] A. Primo, P. Atienzar, E. Sanchez, J.M. Delgado, H. Garcia, From biomass wastes to large-area, high-quality, N-doped graphene: catalyst-free carbonization of chitosan coatings on arbitrary substrates, Chemical Communications, 48 (2012) 9254-9256.

[35] G. Williams, B. Seger, P.V. Kamat, TiO2-graphene nanocomposites. UV-assisted photocatalytic reduction of graphene oxide, Acs Nano, 2 (2008) 1487-1491.
[36] Q. Xiang, J. Yu, M. Jaroniec, Graphene-based semiconductor photocatalysts, Chemical Society Reviews, 41 (2012) 782-796.
[37] H. Zhang, X. Lv, Y. Li, Y. Wang, J. Li, P25-Graphene Composite as a High Performance Photocatalyst, Acs Nano, 4 (2010) 380-386.
[38] J. Albero, E. Dominguez, A. Corma, H. García, Continuous flow photoassisted CO2 methanation, Sustainable Emergy & Fuels, in Press (2017).
[39] M.K. Singh, A. Agarwal, R. Gopal, R.K. Swarnkar, R.K. Kotnala, Dumbbell shaped nickel nanocrystals synthesized by a laser induced fragmentation method, Journal of Materials Chemistry, 21 (2011) 11074-11079.
[40] J.F. Blandez, I. Esteve-Adell, A. Primo, M. Alvaro, H. García, Nickel nanoparticles supported on graphene as catalysts for aldehyde hydrosilylation, Journal of Molecular Catalysis A: Chemical, 412 (2016) 13-19.
[41] M.C. Biesinger, B.P. Payne, L.W.M. Lau, A. Gerson, R.S.C. Smart, X-ray photoelectron spectroscopic chemical state quantification of mixed nickel metal, oxide and hydroxide systems, Surface and Interface Analysis, 41 (2009) 324-332.
[42] G. Elango, S.M. Roopan, K.I. Dhamodaran, K. Elumalai, N.A. Al-Dhabi, M.V. Arasu, Spectroscopic investigation of biosynthesized nickel nanoparticles and its larvicidal, pesticidal activities, Journal of Photochemistry and Photobiology B: Biology, 162 (2016) 162-167.
[43] R. Mahfouz, F.J. Cadete Santos Aires, A. Brenier, B. Jacquier, J.C. Bertolini, Synthesis and physico-chemical characteristics of nanosized particles produced by laser ablation of a nickel target in water, Applied Surface Science, 254 (2008) 5181-5190.
[44] J. Albero, H. Garcia, A. Corma, Temperature Dependence of Solar Light Assisted CO2 Reduction on Ni Based Photocatalyst, Topics in Catalysis, 59 (2016) 787-791.
[45] L. Xu, F. Wang, M. Chen, H. Yang, D. Nie, L. Qi, X. Lian, Alkaline-promoted Ni based ordered mesoporous catalysts with enhanced low-temperature catalytic activity toward CO2 methanation, RSC Advances, 7 (2017) 18199-18210.
[46] F. Sastre, A.V. Puga, L. Liu, A. Corma, H. García, Complete Photocatalytic Reduction of CO2 to Methane by H2 under Solar Light Irradiation, Journal of the American Chemical Society, 136 (2014) 6798-6801.
[47] J. Ren, S. Ouyang, H. Xu, X. Meng, T. Wang, D. Wang, J. Ye, Targeting Activation of CO2 and H2 over Ru-Loaded Ultrathin Layered Double Hydroxides to Achieve Efficient Photothermal CO2 Methanation in Flow-Type System, Advanced Energy Materials, 7 (2017) n/a-n/a.
[48] H.G. Baldoví, M. Álvaro, B. Ferrer, H. García, Photoinduced Charge Separation on the Microsecond Timescale in Graphene Oxide and Reduced Graphene Oxide Suspensions, ChemPhysChem, 17 (2016) 958-962.

Graphical abstract

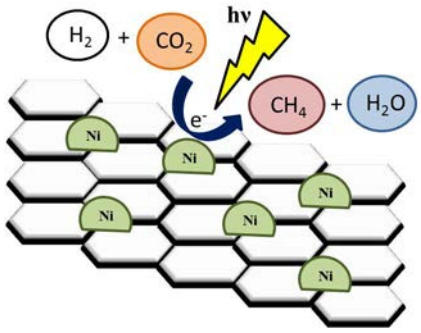

Highlights

- The photocatalytic activity of Ni nanoparticles supported on defective graphene is tested for the photoassisted CO_2 reduction by H_2.
- Under optimal Ni loading of 23 wt%, a maximum specific CH_4 formation rate of 642 $\mu mol/g_{Ni} \cdot h$ and quantum yield of 1.98% are achieved.
- Experimental evidences support that photo-induced charge separation is the most probable mechanism, while temperature is needed to desorb the H_2O produced during reaction.
- Continuous flow operation provides better H_2O desorption from the NiO/Ni-G photocatalyst than batch reaction.